



ARTICLE

Numerical Simulations of Hydromagnetic Mixed Convection Flow of Nanofluids inside a Triangular Cavity on the Basis of a Two-Component Nonhomogeneous Mathematical Model

Khadija A. Al-Hassani¹, M. S. Alam² and M. M. Rahman^{1,*}

¹Department of Mathematics, College of Science, Sultan Qaboos University, Muscat, Oman

²Department of Mathematics, Jagannath University, Dhaka, Bangladesh

*Corresponding Author: M. M. Rahman. Email: mansurdu@yahoo.com; mansur@squ.edu.om

Received: 08 August 2020 Accepted: 24 December 2020

ABSTRACT

Nanofluids have enjoyed a widespread use in many technological applications due to their peculiar properties. Numerical simulations are presented about the unsteady behavior of mixed convection of Fe_3O_4 -water, Fe_3O_4 -kerosene, Fe_3O_4 -ethylene glycol, and Fe_3O_4 -engine oil nanofluids inside a lid-driven triangular cavity. In particular, a two-component non-homogeneous nanofluid model is used. The bottom wall of the enclosure is insulated, whereas the inclined wall is kept a constant (cold) temperature and various temperature laws are assumed for the vertical wall, namely: $\theta = 1$ (Case 1), $\theta = Y(1 - Y)$ (Case 2), and $\theta = \sin(2\pi Y)$ (Case 3). A tilted magnetic field of uniform strength is also present in the fluid domain. From a numerical point of view, the problem is addressed using the Galerkin weighted residual finite element method. The role played by different parameters is assessed, discussed critically and interpreted from a physical standpoint. We find that a higher aspect ratio can produce an increase in the average Nusselt number. Moreover, the Fe_3O_4 -EO and Fe_3O_4 -H₂O nanofluids provide the highest and smallest rate of heat transfer, respectively, for all the considered (three variants of) thermal boundary conditions.

KEYWORDS

Nanofluid; mixed convection; lid-driven; triangular cavity; finite element method

Nomenclature

A :	dimensional amplitude of the wave (m)
AR :	aspect ratio
B_0 :	magnetic field strength ($\text{kg s}^{-2} \text{A}^{-1}$)
c_p :	specific heat at constant pressure ($\text{J kg}^{-1} \text{K}^{-1}$)
C :	nanoparticle volume fraction
D_B :	Brownian diffusion coefficient ($\text{m}^2 \text{s}^{-1}$)
D_T :	thermophoretic diffusion coefficient ($\text{m}^2 \text{s}^{-1}$)
g :	gravitational acceleration (ms^{-1})
H :	height of the cavity (m)
Ha :	Hartmann number
k :	thermal conductivity ($\text{W m}^{-1} \text{K}^{-1}$)
K :	wave number



L :	length of the cavity (m)
Le :	Lewis number
Nb :	Brownian motion parameter
Nr :	buoyancy ratio parameter
Nt :	thermophoresis parameter
Nu :	Nusselt number
p :	dimensional pressure (Pa)
P :	dimensionless pressure
Pr :	Prandtl number
Ri :	Richardson number
T :	temperature (K)
u, v :	dimensional velocity components (ms^{-1})
U, V :	dimensionless velocity components
x, y :	dimensional coordinates (m)
X, Y :	dimensionless coordinates

Greek symbols

α :	thermal diffusivity (m^2s^{-1})
β :	coefficient of thermal expansion (K^{-1})
γ :	magnetic inclination angle (degree)
σ :	electric conductivity ($\text{Wm}^{-1}\text{K}^{-1}$)
θ :	dimensionless temperature
ϕ :	normalized nanoparticle volume fraction
ψ :	stream function (m^2s^{-1})
μ :	dynamic viscosity (Pas)
ρ :	density (kgm^{-3})
(ρc_p) :	heat capacity ($\text{JK}^{-1}\text{m}^{-3}$)

Subscripts

ave:	average
c:	condition at cold wall
f:	base fluid
h:	condition at heated wall
p:	solid nanoparticle

1 Introduction

The overheating limits the lifespan of the usage of electronic pieces of equipment (for example, computer processor) while operating. It is a big challenge for the industries which produce such sophisticated types of equipment. In a recent study, Bayomy et al. [1] reported that the efficiency rate of electronic devices decreases exponentially due to heat generation within them. The traditional fluids (water, mineral oils, and ethylene glycol) most of the time used for industrial cooling applications limit their use as efficient heat transfer agent. For the growing need in modern technology (chemical production, power station, a computer processor, and micro-electronics), researchers developed nanofluid [2], which efficiently transmit heat. Nanofluid exhibits higher thermal conductivity hence enhanced heat transfer compared to the conventional fluids [3–13] even in the presence of a small amount (1%–5% volume fraction) of nanoparticles.

The heat transfer enhancement inside cavities has become a paramount issue in the industrial and energy sectors. Many researchers studied nanofluids experimentally, analytically as well as numerically for heat enhancement in cavities. In this respect, Khanafer et al. [14] studied the heat transfer enhancement in a differentially heated square cavity. They found that the suspended nanoparticles considerably increase the heat transfer rate. Oztop et al. [15] conducted a numerical study considering the natural convection flow inside the partially heated rectangular enclosure filled with nanofluids. They found that the mean Nusselt number increases with the increase of the nanoparticles volume fraction. They further reported that the low aspect ratio of the geometry significantly enhances the heat transfer rate in nanofluids compared to the corresponding heat transfer for a high aspect ratio.

Magnetohydrodynamics (MHD) convective flow has widespread applications in science and engineering such as extraction of geothermal energy, oil recovery from the petroleum reservoirs, thermal insulation, cooling of nuclear reactors, crystal growth, and plasma confinement [16–18]. In light of the various applications of MHD and nanofluids, Al Kalbani et al. [19,20] investigated the buoyancy induced heat transfer flow inside a tilted square cavity filled with nanofluids in the presence of an oriented magnetic field. Their results confirm that the nanoparticle volume fraction, shape, and size significantly intensified the heat transfer rate inside a crater. The applied magnetic field and its direction also played a vital role in heat enhancement. Al Balushi et al. [21,22] further investigated the free convection heat transfer flow of nanofluids inside square cavities utilizing nanofluids under the action of an applied inclined magnetic field to the flow domain. They used a nonhomogeneous dynamic model for nanofluid modeling. They found that heat enhancement in nanofluids depends on the nanoparticle loading, magnetic field's direction and strength, and the location of the heater that supplies heat to the flow field.

The thermal discharge in lid-driven enclosures has direct applications in many engineering fields such as in rheology for lubrication mechanisms, cooling of electronic devices, constructing buildings roofs and attics, processing food, and cooling nuclear reactors (see [23]). Flack et al. [24,25] studied experimentally as well as numerically the convective heat transfer in triangular enclosures. Later on, many researchers conducted research and reported results on triangular-cavities [26–31]. All of these studies involved heat transfer in regular fluids. Due to the growing need for nanofluid research in triangular cavities, Ghasemi et al. [32] studied numerically; the steady natural convection flow of CuO-water nanofluid inside a fixed-walls right triangular enclosure. They reported that the Brownian motion of nanoparticles takes part in enhancing the thermal performance of nanofluids in a cavity. Ghasemi et al. [33] further studied steady mixed convection in a lid-driven triangular enclosure filled with Al₂O₃-water nanofluid. They confirmed that enhancement in heat transfer within the cavity is due to the addition of nanoparticles, and it depends on the direction of the sliding wall motion. Rahman et al. [34] conducted a numerical study on hydromagnetic free convection flow of nanofluids inside an isosceles-triangular cavity. In their simulation, they used the two-component nonhomogeneous mathematical model and different thermal conditions. The results show that the variable thermal boundary conditions have significant effects on the flow and thermal fields. Rahman [35] studied the hydromagnetic natural convection flow and heat transfer within an equilateral triangular enclosure. In his work, he used water-based as well as kerosene-based ferrofluids in the presence of a sloping magnetic field. The results indicate that increased magnetic field strength diminishes the heat transfer rate, whereas it enhances with the increment of the magnetic field inclination angle. Rahman [36] further studied steady heat transfer in Fe₃O₄-water nanofluid inside a triangular cavity with fixed walls under a sloping magnetic field. They conclude that a higher degree of heat transfer is accomplished by reducing the dimension of nanoparticles and increasing the strength of the buoyancy force. Azam et al. [37–41] published a series of papers on unsteady heat and mass transfer flow of nanofluids in different geometries with the various flow and thermal conditions proposed by the Buongiorno mathematical model. In a recent study, Uddin et al. [42] explored heat transportation in copper oxide-water nanofluid inside different triangular cavities. Their results show that heat

enhancement in nanofluids strongly depends on the shape of the triangular shape cavity and the applied buoyancy force.

Despite significant research studies on various cavities reported in the literature, there is a substantial lack of information regarding the problem of time-dependent hydromagnetic fluid flow and heat transfer enhancement in the lid-driven right triangular-cavity filled with nanofluids. Therefore, the present paper aims to investigate numerically unsteady mixed convection flow and heat transfer in a lid-driven right-triangular cavity filled with different types of nanofluids in the presence of an oriented magnetic field varying aspect ratio of the enclosure taking into account the Buongiorno mathematical model. We used the Galerkin weighted residual-based finite element method for numerical simulation. Finally, we depicted the mean rate of heat transfer in terms of Nusselt number in varying different model parameters. The organization of the remainder of the paper is as follows: In Section 2, we formulate the problem physically as well as mathematically. Section 3 explains the method of solution in detail. The numerical outcomes we discuss from physical and engineering viewpoints in Section 4. In the end, in Section 5, we conclude our study.

2 Problem Formulation

2.1 Physical Modeling

We consider an unsteady, laminar, incompressible two-dimensional mixed convection flow inside a right-angle triangular cavity that is filled with Fe_3O_4 -water nanofluid as shown in Fig. 1, where x and y are the Cartesian coordinates. Here, L is the bottom wall length, and H is the height of the vertical wall. We assumed that the vertical wall temperature is T_h while the inclined wall (hypotenuse) is T_c (where $T_h > T_c$). The bottom-wall is insulated; thus, no heat can escape along the transverse direction of it. Initially, we considered that nanofluid concentration is C_C , but for $t > 0$, it is assumed as C_h in the entire domain so that $C_h > C_C$. The vertical wall is allowed to move with constant speed V_0 in its plane while the remaining walls have no speed. Here the gravity acts in the vertical direction, along the y -axis. We included the thermophoresis and Brownian diffusion effects in the mathematical model in the absence of any chemical reaction and thermal radiation. The base fluid and the nanoparticles are in thermal equilibrium, and hence no slip occurs between them. Surfactant or surface charge technology disperses the nanoparticles within the nanofluid. The Boussinesq approximation tackled the density variation in the buoyancy force.

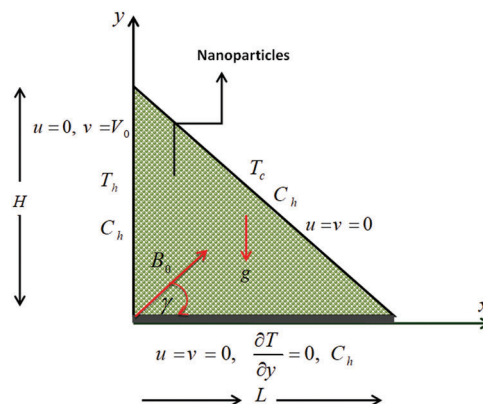


Figure 1: Schematic view of the physical model with boundary conditions

The cavity is permeated by a uniform magnetic field $\mathbf{B} = B_x \mathbf{i} + B_y \mathbf{j}$ of constant magnitude $B_0 = \sqrt{B_x^2 + B_y^2}$, where \mathbf{i} and \mathbf{j} are the unit vectors along the coordinate axes. Also, the direction of the magnetic field makes an angle γ with the positive x -axis. We may use this type of cavity filled with nanofluid to model a solar thermal collector.

2.2 Mathematical Modeling

Within the framework of the above-noted assumptions, the governing conservation equations for this model are expressed in dimensional form as follows [9,34–36]:

$$\frac{\partial u}{\partial x} + \frac{\partial v}{\partial y} = 0 \quad (1)$$

$$\frac{\partial u}{\partial t} + u \frac{\partial u}{\partial x} + v \frac{\partial u}{\partial y} = -\frac{1}{\rho_f} \frac{\partial p}{\partial x} + \nu_f \nabla^2 u + \frac{\sigma_f B_0^2}{\rho_f} (v \sin \gamma \cos \gamma - u \sin^2 \gamma) \quad (2)$$

$$\begin{aligned} \frac{\partial v}{\partial t} + u \frac{\partial v}{\partial x} + v \frac{\partial v}{\partial y} = & -\frac{1}{\rho_f} \frac{\partial p}{\partial y} + \nu_f \nabla^2 v + \frac{\sigma_f B_0^2}{\rho_f} (u \sin \gamma \cos \gamma - v \cos^2 \gamma) \\ & + \frac{1}{\rho_f} [(1 - C_c)(T - T_c) \rho_f \beta_f g - (C - C_c)(\rho_p - \rho_f) g] \end{aligned} \quad (3)$$

$$\frac{\partial T}{\partial t} + u \frac{\partial T}{\partial x} + v \frac{\partial T}{\partial y} = \alpha_f \nabla^2 T + \frac{(\rho c_p)_p}{(\rho c_p)_f} D_B \left(\frac{\partial T}{\partial x} \frac{\partial C}{\partial x} + \frac{\partial T}{\partial y} \frac{\partial C}{\partial y} \right) + \frac{(\rho c_p)_p}{(\rho c_p)_f} \frac{D_T}{T_c} \left[\left(\frac{\partial T}{\partial x} \right)^2 + \left(\frac{\partial T}{\partial y} \right)^2 \right] \quad (4)$$

$$\frac{\partial C}{\partial t} + u \frac{\partial C}{\partial x} + v \frac{\partial C}{\partial y} = D_B \nabla^2 C + \frac{D_T}{T_c} \nabla^2 T \quad (5)$$

where $\nabla^2 = \frac{\partial^2}{\partial x^2} + \frac{\partial^2}{\partial y^2}$ and the descriptions of the physical variables are mentioned in the nomenclature.

2.3 Initial and Boundary Conditions

The appropriate initial and boundary conditions for the above-stated model are as follows:

1) For $t \leq 0$:

$$u = v = 0, T = T_c, C = C_c, p = 0, 0 \leq x \leq L, 0 \leq y \leq H \quad (6)$$

2) For $t > 0$:

$$(a) \text{ On the vertical wall } (x = 0, 0 \leq y \leq H): u = 0, v = V_0, T = T_h, C = C_h \quad (7)$$

$$(b) \text{ On the bottom wall } (0 \leq x \leq L, y = 0): u = 0, v = 0, \frac{\partial T}{\partial y} = 0, C = C_h \quad (8)$$

$$(c) \text{ On the inclined wall } \left(\frac{x}{L} + \frac{y}{H} = 1 \right): u = 0, v = 0, T = T_c, C = C_h \quad (9)$$

2.4 Introduction of Non-Dimensional Variables

The governing differential Eqs. (1)–(5) representing conservation laws are rarely solved using dimensional variables. The common practice is to write these dimensional equations in a non-dimensional form using dimensionless quantities obtained through proper characteristics scales. Writing the conservation equations in non-dimensional forms results in dimensionless numbers that are very useful

for performing parametric studies of engineering problems. Again, the use of non-dimensional variables has several advantages. It allows reducing the number of appropriate parameters for the problem considered, revealing the relative magnitude of the various terms in the conservation equation that are less important. This process simplifies the equation to be solved and leaves only the terms of a similar order of magnitude, which results in better numerical accuracy. Besides, the generated solution will apply to all dynamically similar-problems. A dimensional variable is transformed into a non-dimensional one by dividing the variable by a quantity (composed of one or more physical properties) having the same dimension as the original variable. Thus the non-dimensional forms of the governing conservation Eqs. (1)–(5) together with the initial and boundary conditions (6)–(9) are obtained by employing the following dimensionless parameters:

$$\begin{aligned} X &= \frac{x}{L}, Y = \frac{y}{L}, U = \frac{u}{V_0}, V = \frac{v}{V_0}, \tau = \frac{tV_0}{L}, \\ P &= \frac{p}{V_0^2 \rho_f}, \theta = \frac{T - T_c}{T_h - T_c}, \phi = \frac{C - C_c}{C_h - C_c} \end{aligned} \quad (10)$$

Substituting (10) into (1)–(5), we obtain the dimensionless equations as follows:

$$\frac{\partial U}{\partial X} + \frac{\partial V}{\partial Y} = 0 \quad (11)$$

$$\frac{\partial U}{\partial \tau} + U \frac{\partial U}{\partial X} + V \frac{\partial U}{\partial Y} = -\frac{\partial P}{\partial X} + \frac{1}{\text{Re}} \left(\frac{\partial^2 U}{\partial X^2} + \frac{\partial^2 U}{\partial Y^2} \right) + \frac{Ha^2}{\text{Re}} (V \sin \gamma \cos \gamma - U \sin^2 \gamma) \quad (12)$$

$$\begin{aligned} \frac{\partial V}{\partial \tau} + U \frac{\partial V}{\partial X} + V \frac{\partial V}{\partial Y} &= -\frac{\partial P}{\partial Y} + \frac{1}{\text{Re}} \left(\frac{\partial^2 V}{\partial X^2} + \frac{\partial^2 V}{\partial Y^2} \right) \\ &+ \frac{Ha^2}{\text{Re}} (U \sin \gamma \cos \gamma - V \cos^2 \gamma) + Ri[\theta - Nr\phi] \end{aligned} \quad (13)$$

$$\begin{aligned} \frac{\partial \theta}{\partial \tau} + U \frac{\partial \theta}{\partial X} + V \frac{\partial \theta}{\partial Y} &= \frac{1}{\text{RePr}} \left(\frac{\partial^2 \theta}{\partial X^2} + \frac{\partial^2 \theta}{\partial Y^2} \right) \\ &+ \frac{Nb}{\text{RePr}} \left(\frac{\partial \phi}{\partial X} \frac{\partial \theta}{\partial X} + \frac{\partial \phi}{\partial Y} \frac{\partial \theta}{\partial Y} \right) + \frac{Nt}{\text{RePr}} \left[\left(\frac{\partial \theta}{\partial X} \right)^2 + \left(\frac{\partial \theta}{\partial Y} \right)^2 \right] \end{aligned} \quad (14)$$

$$\frac{\partial \phi}{\partial \tau} + U \frac{\partial \phi}{\partial X} + V \frac{\partial \phi}{\partial Y} = \frac{1}{\text{RePrLe}} \left(\frac{\partial^2 \phi}{\partial X^2} + \frac{\partial^2 \phi}{\partial Y^2} \right) + \frac{Nt}{Nb\text{RePrLe}} \left(\frac{\partial^2 \theta}{\partial X^2} + \frac{\partial^2 \theta}{\partial Y^2} \right) \quad (15)$$

The non-dimensional boundary conditions become

1. For $\tau \leq 0$:

$$U = V = 0, \theta = 0, \phi = 0, P = 0; 0 \leq X, 0 \leq Y, X + \frac{Y}{AR} \leq 1 \quad (16)$$

2. For $\tau > 0$:

$$(a) \text{ On the vertical wall } (X = 0, 0 \leq Y \leq AR): U = 0, V = 1, \theta = 1, \phi = 1 \quad (17)$$

$$(b) \text{ On the bottom wall } (0 \leq X \leq 1, Y = 0): U = 0, V = 0, \frac{\partial \theta}{\partial Y} = 0, \phi = 1 \quad (18)$$

$$(c) \text{ On the inclined wall } (X + \frac{Y}{AR} = 1): U = 0, V = 0, \theta = 0, \phi = 1 \quad (19)$$

The parameters appeared in (11)–(19) are defined by

$$AR = \frac{H}{L} \text{ is the aspect ratio of the triangular enclosure, } Pr = \frac{\nu_f}{\alpha_f} \text{ is the Prandtl number, } Ha = B_0 L \sqrt{\frac{\sigma_f}{\mu}} \text{ is the Hartmann number, } Re = \frac{V_0 L}{\nu_f} \text{ is the Reynolds number, } Le = \frac{\alpha_f}{D_B} \text{ is the Lewis number, } Gr = \frac{g \beta_f L^3 (1 - C_c) \Delta T}{\nu_f} \text{ is the Grashof number, } Ri = \frac{Gr}{Re^2} \text{ is the Richardson number, } Nr = \frac{\Delta C (\rho_p - \rho_f)}{\Delta T \beta_f \rho_f (1 - C_c)} \text{ is the buoyancy ratio parameter, } Nt = \frac{(\rho c_p)_p D_T \Delta T}{(\rho c_p)_f T_c \alpha_f} \text{ is the thermophoresis parameter, and } Nb = \frac{(\rho c_p)_p D_B \Delta C}{(\rho c_p)_f \alpha_f} \text{ is the Brownian diffusion parameter.}$$

The dimensionless Eqs. (11)–(15) determine the physical parameters that affect the solutions. The role of these parameters on the flow and thermal fields are discussed in the results and discussion section.

2.5 Average Nusselt Number

The significant physical quantity in this model is the calculation of the average Nusselt number Nu_{ave} along the left heated wall. The Nusselt number Nu is the ratio of convective to conductive heat transfer across the boundary, and the local Nusselt number is defined by

$$Nu_L = \frac{hH}{\kappa_f \Delta T} \quad (20)$$

where $\Delta T = T_h - T_c$, H is the height of the triangle (the vertical heated wall), κ_f is the thermal conductivity of the base fluid. The convective heat transfer coefficient of the nanofluid flow h is defined by

$$h = -\kappa_f \frac{\partial}{\partial x} (T - T_c) \quad (21)$$

Using the dimensionless variables defined in Eq. (10), the heat transfer coefficient of nanofluid at the left heated wall turns into

$$h = -\frac{\kappa_f \Delta T}{L} \left(\frac{\partial \theta}{\partial X} \right)_{X=0} \quad (22)$$

Hence, the local Nusselt number for nanofluid at the left heated wall can be expressed as

$$Nu_L = -AR \left(\frac{\partial \theta}{\partial X} \right)_{X=0} \quad (23)$$

The average Nusselt number is expressed as follows:

$$Nu_{ave} = -\int_0^{AR} \left(\frac{\partial \theta}{\partial X} \right)_{X=0} dY \quad (24)$$

3 Numerical Procedure

We applied the Galerkin weighted residual-based finite element method (FEM) to solve the governing dimensionless Eqs. (11)–(15) and boundary conditions (17)–(19). A finite element method is a numerical tool that approximates the solution of boundary value problems of partial differential equations. The finite element method exhibits high accuracy of calculation and easily handles complex geometries in engineering problems. In FEM, we construct approximation functions using the weighted-integral technique to find a solution of differential equations. We accomplished this by dividing the whole domain into a set of small sub-domains called finite elements. These elements can be of different types. In 2D problems, we usually use either triangular or quadrilateral shape elements. Besides, in 3D, the most commonly used elements' shape is tetrahedral or hexahedral. Here, we used six node triangular shape elements for developing the finite element equations. All six nodes are connected with velocities, temperature, and concentration fields, while only the corner nodes are associated with pressure. In the finite element method, the approximate solutions are expressed in terms of the shape (or interpolation) functions, which can be linear or quadratic depending on the number of nodes per element. Also, in 2D problems, the x , y - coordinates (global coordinate) are mapped into ξ , η coordinates (or local coordinates), and the shape functions are defined as functions of ξ and η . Such local coordinates (ξ , η) are useful in the numerical evaluation of the integration. Now in terms of local coordinates, the quadratic shape functions for the velocities, temperature, and concentration are as follows:

$$\left. \begin{aligned} Q_1(\xi, \eta) &= \frac{1}{2}(\xi + \eta)(\xi + \eta + 1), Q_2(\xi, \eta) = -(\xi + 1)(\xi + \eta) \\ Q_3(\xi, \eta) &= \frac{1}{2}\xi(\xi + 1), Q_4(\xi, \eta) = (\xi + 1)(\eta + 1) \\ Q_5(\xi, \eta) &= \frac{1}{2}\eta(\eta + 1), Q_6(\xi, \eta) = -(\eta + 1)(\xi + \eta) \end{aligned} \right\} \quad (25)$$

where

$$Q_i(\xi, \eta) = \begin{cases} 1 & \text{at node } i \\ 0 & \text{at every other node} \end{cases} \quad (26)$$

and

$$\sum_{i=1}^6 Q_i(\xi, \eta) = 1 \text{ for all } \xi, \eta \text{ in } -1 \leq \xi \leq 1 \text{ and } -1 \leq \eta \leq 1 \quad (27)$$

Also, the linear shape functions for the pressure are as follows:

$$L_1(\xi, \eta) = -\frac{1}{2}(\xi + \eta), L_2(\xi, \eta) = \frac{1}{2}(1 + \xi), L_3(\xi, \eta) = \frac{1}{2}(1 + \eta) \quad (28)$$

with the property

$$L_i(\xi, \eta) = \begin{cases} 1 & \text{at node } i \\ 0 & \text{at every other node} \end{cases} \quad (29)$$

and

$$\sum_{i=1}^3 L_i(\xi, \eta) = 1 \text{ for all } \xi, \eta \text{ in } -1 \leq \xi \leq 1 \text{ and } -1 \leq \eta \leq 1 \quad (30)$$

Again, for the triangular shape element, the coordinates x, y can be represented in terms of nodal coordinates using the same shape functions and this is known as isoparametric representation. Thus, for isoparametric representation, the transformation between (x, y) and (ξ, η) is accomplished by a coordinate transformation of the form

$$x = \sum_{i=1}^6 x_i Q_i(\xi, \eta), \quad y = \sum_{i=1}^6 y_i Q_i(\xi, \eta) \quad (31)$$

In the 2D problem discussed here, each node is permitted to displace along with the two directions, x and y . Thus, each node has two degrees of freedom. As a result, the number of unknown variables for velocities, temperature, concentration, and pressure is 27 per element, and hence there are 27 degrees of freedom. Thus, in terms of the above-defined shape functions, the approximate solutions of U, V, θ, ϕ and P can be expressed as follows:

$$\left. \begin{aligned} U(X, Y, \tau) &= \sum_{i=1}^6 U_i(\tau) Q_i(\xi, \eta), \quad V(X, Y, \tau) = \sum_{i=1}^6 V_i(\tau) Q_i(\xi, \eta), \quad \theta(X, Y, \tau) = \sum_{i=1}^6 \theta_i(\tau) Q_i(\xi, \eta), \\ \phi(X, Y, \tau) &= \sum_{i=1}^6 \phi_i(\tau) Q_i(\xi, \eta), \quad P(X, Y) = \sum_{i=1}^3 P_i L_i(\xi, \eta) \end{aligned} \right\} \quad (32)$$

where $U_i, V_i, \theta_i, \phi_i$ and P_i are the corresponding nodal values of the unknown functions.

In the Galerkin weighted residual-based finite element method, the weight functions that we choose are the same as the shape functions that have been used in the approximate solutions (32). Thus employing the Galerkin weighted residual approach on Eqs. (11)–(15) and also using the Gauss's divergence theorem on the second derivative terms that contain in Eqs. (12)–(15), we get finally, the following finite element equations:

$$\int_{\Omega^e} Q_i \left(\frac{\partial U}{\partial X} + \frac{\partial V}{\partial Y} \right) d\Omega^e = 0 \quad (33)$$

$$\begin{aligned} & \int_{\Omega^e} Q_i \left(\frac{\partial U}{\partial \tau} + U \frac{\partial U}{\partial X} + V \frac{\partial U}{\partial Y} \right) d\Omega^e + \int_{\Omega^e} L_i \frac{\partial P}{\partial X} d\Omega^e + \frac{1}{\text{Re}} \int_{\Omega^e} \left(\frac{\partial Q_i}{\partial X} \frac{\partial U}{\partial X} + \frac{\partial Q_i}{\partial Y} \frac{\partial U}{\partial Y} \right) d\Omega^e \\ & - \frac{Ha^2}{\text{Re}} \int_{\Omega^e} Q_i (V \sin \gamma \cos \gamma - U \sin^2 \gamma) d\Omega^e - \frac{1}{\text{Re}} \int_{\Gamma^e} Q_i S_x ds = 0 \end{aligned} \quad (34)$$

$$\begin{aligned} & \int_{\Omega^e} Q_i \left(\frac{\partial V}{\partial \tau} + U \frac{\partial V}{\partial X} + V \frac{\partial V}{\partial Y} \right) d\Omega^e + \int_{\Omega^e} L_i \frac{\partial P}{\partial Y} d\Omega^e + \frac{1}{\text{Re}} \int_{\Omega^e} \left(\frac{\partial Q_i}{\partial X} \frac{\partial V}{\partial X} + \frac{\partial Q_i}{\partial Y} \frac{\partial V}{\partial Y} \right) d\Omega^e \\ & - \frac{Ha^2}{\text{Re}} \int_{\Omega^e} Q_i (U \sin \gamma \cos \gamma - V \cos^2 \gamma) d\Omega^e - Ri \int_{\Omega^e} Q_i [\theta - Nr\phi] d\Omega^e - \frac{1}{\text{Re}} \int_{\Gamma^e} Q_i S_y ds = 0 \end{aligned} \quad (35)$$

$$\begin{aligned} & \int_{\Omega^e} Q_i \left(\frac{\partial \theta}{\partial \tau} + U \frac{\partial \theta}{\partial X} + V \frac{\partial \theta}{\partial Y} \right) d\Omega^e + \frac{1}{\text{RePr}} \int_{\Omega^e} \left(\frac{\partial Q_i}{\partial X} \frac{\partial \theta}{\partial X} + \frac{\partial Q_i}{\partial Y} \frac{\partial \theta}{\partial Y} \right) d\Omega^e - \frac{1}{\text{RePr}} \int_{\Gamma^e} Q_i q_w ds \\ & - \frac{Nb}{\text{RePr}} \int_{\Omega^e} Q_i \left(\frac{\partial \phi}{\partial X} \cdot \frac{\partial \theta}{\partial X} + \frac{\partial \phi}{\partial Y} \cdot \frac{\partial \theta}{\partial Y} \right) d\Omega^e - \frac{Nt}{\text{RePr}} \int_{\Omega^e} Q_i \left[\left(\frac{\partial \theta}{\partial X} \right)^2 + \left(\frac{\partial \theta}{\partial Y} \right)^2 \right] d\Omega^e = 0 \end{aligned} \quad (36)$$

$$\int_{\Omega^e} Q_i \left(\frac{\partial \phi}{\partial \tau} + U \frac{\partial \phi}{\partial X} + V \frac{\partial \phi}{\partial Y} \right) d\Omega^e + \frac{1}{\text{RePrLe}} \int_{\Omega^e} \left(\frac{\partial Q_i}{\partial X} \frac{\partial \phi}{\partial X} + \frac{\partial Q_i}{\partial Y} \frac{\partial \phi}{\partial Y} \right) d\Omega^e + \frac{Nt}{Nb\text{RePrLe}} \int_{\Omega^e} \left(\frac{\partial Q_i}{\partial X} \frac{\partial \theta}{\partial X} + \frac{\partial Q_i}{\partial Y} \frac{\partial \theta}{\partial Y} \right) d\Omega^e - \frac{1}{\text{RePrLe}} \int_{\Gamma^e} Q_i q_{2w} ds = 0 \quad (37)$$

Here, Ω^e is the typical triangular element area, Γ^e is the boundary of the element Ω^e , ds is the arc length of an infinitesimal line element along the boundary Γ^e , $\mathbf{n} = (\mathbf{n}_x, \mathbf{n}_y)$ is the unit outward normal vector on the boundary Γ^e , S_x and S_y are the outflows from the boundary along the x and y - directions respectively. $q_w = \nabla \theta \cdot \mathbf{n}$ denotes the heat flux normal to the boundary of the element and $q_{2w} = \nabla \theta \cdot \mathbf{n} + \nabla \phi \cdot \mathbf{n}$ is the sum of heat and mass fluxes which are normal to the boundary of the element Ω^e .

We used a three-point Gaussian quadrature formula to evaluate the integrals in the residual Eqs. (33)–(37). Using the Newton-Raphson method, non-linear residual Eqs. (33)–(37) are solved to determine the coefficients of the expansions in Eq. (32). The details of this technique are well documented in the textbook by Reddy et al. [43]. The readers can also consult the work of Uddin et al. [44]. We set $|\Gamma^{r+1} - \Gamma^r| \leq 10^{-5}$, where Γ is the general dependent variable (U , V , θ , ϕ), and r is the number of iteration in order to calculate the error and to determine the convergence of the solution. We tabulated the thermophysical properties of the base fluids and nanoparticles in Tab. 1.

Table 1: Thermo-physical properties of the base fluids and nanoparticles (see [15])

Thermophysical properties	H ₂ O	EO	Ke	EG	Fe ₃ O ₄
C_p (Jkg ⁻¹ K ⁻¹)	4179	1880.3	2090	2382.1	670
ρ (kgm ⁻³)	997.1	888.23	780	1117.48	5180
κ (Wm ⁻¹ K ⁻¹)	0.613	0.145	0.149	0.2492	80.4
μ (Pas)	0.001003	0.8451	0.00164	0.022	–
$\beta \times 10^{-5}$ (K ⁻¹)	21	70	99	57	20.6
$\alpha \times 10^{-7}$ (m ² s ⁻¹)	1.47	0.868	0.914	0.94868	231.17
Pr	6.8377	10959	23.004	210.2978	–

3.1 Test for Grid Independence

The scrutiny of grid sensitivity on a converged solution is essential for the correct usage of the finite element method. Here, we examined five non-uniform grids named coarse, normal, fine, finer, and extra-fine. Each of them has 297, 668, 1075, 1643, and 7435 number of elements within the resolution field. We have calculated the average Nusselt number (Nu_{ave}) for the afore-said mesh elements and tabulated in Tab. 2 for understanding grid fineness. From Tab. 2, we notice that the values of the average Nusselt number for 1643 and 7435 mesh elements remain almost the same. It indicates that either 1643 or 7435 mesh elements are sufficient to obtain a grid-independent solution. To save run time and memory, we used 1643 mesh elements for numerical computation.

Table 2: Grid sensitivity check for Fe₃O₄-water nanofluid when $Ri = 10^4$, $Pr = 6.8377$, $Nb = 1.24 \times 10^{-5}$, $Nt = 9.58 \times 10^{-7}$, $Le = 16795$, $Ha = 25$, $\gamma = 15^\circ$, and $AR = 1$

Number of nodes	175	374	588	884	3850
Number of elements	297	668	1075	1643	7435
Nu_{ave}	9.0643	9.7321	10.2874	10.3905	10.3906

3.2 Code Validation

We tallied our simulated results with the work of Ghasemi et al. [33]. They studied a mixed convection flow in a lid-driven right-angled triangular cavity in the absence of mass transfer. They have considered the insulated horizontal wall, hot inclined wall, and uniformly moving cold vertical wall. In Tab. 3, we compared our calculated average Nusselt number with Ghasemi et al. [33] varying Richardson number, Ri . The comparisons show an excellent agreement among the data and inspire us to use the current code.

Table 3: Comparison of average Nusselt numbers Nu_{ave} with those of Ghasemi et al. [33] when $Ha = 0$, $Nr = 0$, $Nb = 0$ and $Nt = 0$ in the present model

Ri	Ghasemi et al. [33]	Present results	% of Error
0.01	33.275	33.276	3.0×10^{-3}
0.1	29.356	29.357	3.4×10^{-3}
1	11.073	11.074	9.0×10^{-3}
10	11.073	11.074	9.0×10^{-3}
100	11.318	11.320	1.7×10^{-2}

4 Numerical Results and Discussion

In this section, we mainly presented average Nusselt numbers computed for different values of the model parameters. Due to the Brownian diffusion and thermophoresis, it is expected that there is a minimal concentration difference say, $\Delta C = 0.01$ within the flow field. For Fe_3O_4 nanoparticle with diameter $d_p = 50$ nm, and assuming reference temperature $T_c = 300$ K, temperature difference $\Delta T = 10$ K, the Brownian diffusion and thermophoresis coefficients are calculated as $D_B = 8.7591 \times 10^{-12}$ and $D_T = 3.9597 \times 10^{-12}$ respectively (see [44,45]). The corresponding values for the other physical parameters are $Pr = 6.8377$, $Nb = 1.24 \times 10^{-5}$, $Nt = 9.58 \times 10^{-7}$, and $Le = 16795$. It is good mention that in nanofluid research using Buongiorno model, the values of the Brownian diffusion parameter Nb , thermophoresis parameter, and Lewis number are very poorly determined in a significant number of studies in the open literature (see [46]). In our simulation, we have used the realistic values of the aforesaid-parameters, which make this study unique. For numerical computation, we considered $Ri = 10^4$, $Pr = 6.838$, $Ha = 25$, $\gamma = 15^\circ$, $Nb = 1.24 \times 10^{-5}$, $Nt = 9.58 \times 10^{-7}$, $Nr = 0.001$, $Le = 16795$, and $AR = 1$ as default unless otherwise specified.

To explore the time progression of numerical solutions, we have calculated the streamlines of Fe_3O_4 -water nanofluid for different values of the dimensionless time τ keeping other model parameter values fixed. We have taken the snapshot of the unsteady solution at $\tau = 0.01, 0.1, 1$, and 1.5 and depicted in Fig. 2. This series of figures show the time progression of solutions from the transient state to a steady state. We can see that when $\tau \geq \tau_s = 1$, there are no changes in the structure of streamlines, which means that the solution reached a steady-state. As dimensionless time increases, the fluid flow intensity increases and approaches a steady-state.

Fig. 3 shows the dimensionless time τ_s needed to reach the solution in a steady-state for different Richardson number Ri . We detected that for increasing Richardson's number the solution requires more time to be in a steady-state. It is because increased Ri weakens inertia force over the buoyancy force as a result of the external driving force, the nanofluid motion diminishes. Hence, the system required more time to be in a steady-state.

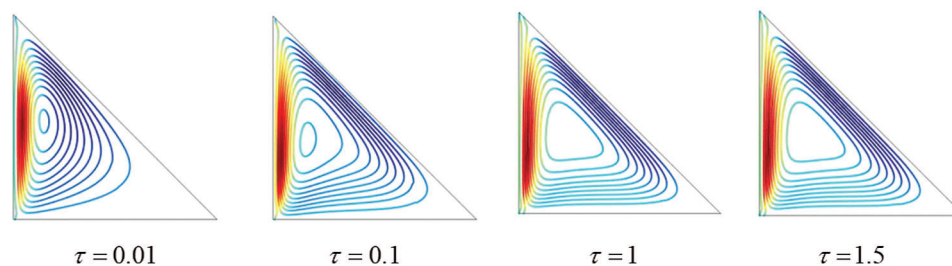


Figure 2: Streamlines for Fe_3O_4 -water nanofluid for different dimensionless time (τ) when $Ri = 10^5$, $Pr = 6.838$, $Nb = 1.24 \times 10^{-5}$, $Nt = 9.58 \times 10^{-7}$, $Nr = 0.001$, $Le = 16795$, $Ha = 25$, $\gamma = 15^\circ$ and $AR = 1$

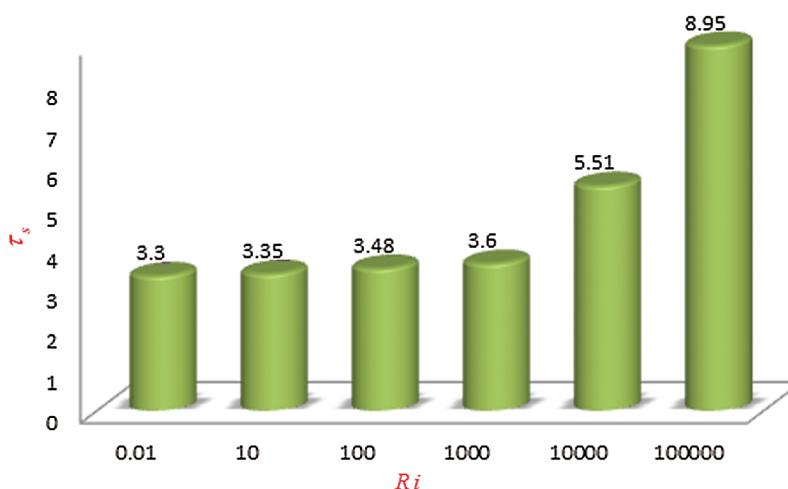


Figure 3: Dimensionless time τ_s needed to reach the solution in steady state for different Ri when $Pr = 6.838$, $Nb = 1.24 \times 10^{-5}$, $Nt = 9.58 \times 10^{-7}$, $Nr = 0.001$, $Le = 16795$, $Ha = 25$, $\gamma = 15^\circ$, $AR = 1$

Figs. 4(a)–4(c), respectively, illustrate the average Nusselt number Nu_{ave} , i.e., the rate of heat transfer from the hot surface (left vertical wall of the cavity) to the nanofluid for different values of the (a) Richardson number Ri , (b) Hartmann number Ha as well as (c) magnetic field orientation angle γ concerning various dimensionless time τ_s . The variation in average Nusselt number against dimensionless time shows the evolution of solution from the unsteady-state to the steady-state. The average Nusselt number Nu_{ave} is very-large, near $\tau = 0.01$, due to the sudden increase in temperature at the vertical wall. The average Nusselt number decreases with time and approaches a steady-state after a certain-time $\tau \geq \tau_s$. Also, it can be seen that as the Richardson number increases, the average Nusselt number also increases due to the natural convection. From these figures, we observe that higher values of the Hartmann number, as well as the magnetic field inclination angle, forced the solution to reach a steady-state earlier compared to the absence of the magnetic field within the flow domain. We also found that the heat transfer rate decreases with the increase of the values of τ , whereas when the Hartmann number Ha , as well as the magnetic field inclination angle, increases, the rate of heat transfer decreases.

Fig. 5 shows the average Nusselt number for different Hartmann number Ha with various values of the Richardson number Ri . As clearly seen, for $Ri < 100$, the heat is transferred inside the enclosure by conduction and the convection mode of heat transfer starts when $Ri > 100$. When the Hartmann number is zero ($Ha = 0$) or when the effect of the magnetic field is absent, the average Nusselt number increases sharply. In this case, the buoyancy force due to the natural convection effect is the only dominant force in

the enclosure. When the Hartmann number increases, the Lorentz force becomes energetic and dominates over the buoyancy force that causes a reduction the heat transfer for all considered values of Ri . It means that a stronger magnetic field may delay the onset of convection. Thus, the rate of heat transfer can be controlled by controlling the strength of the applied magnetic field.

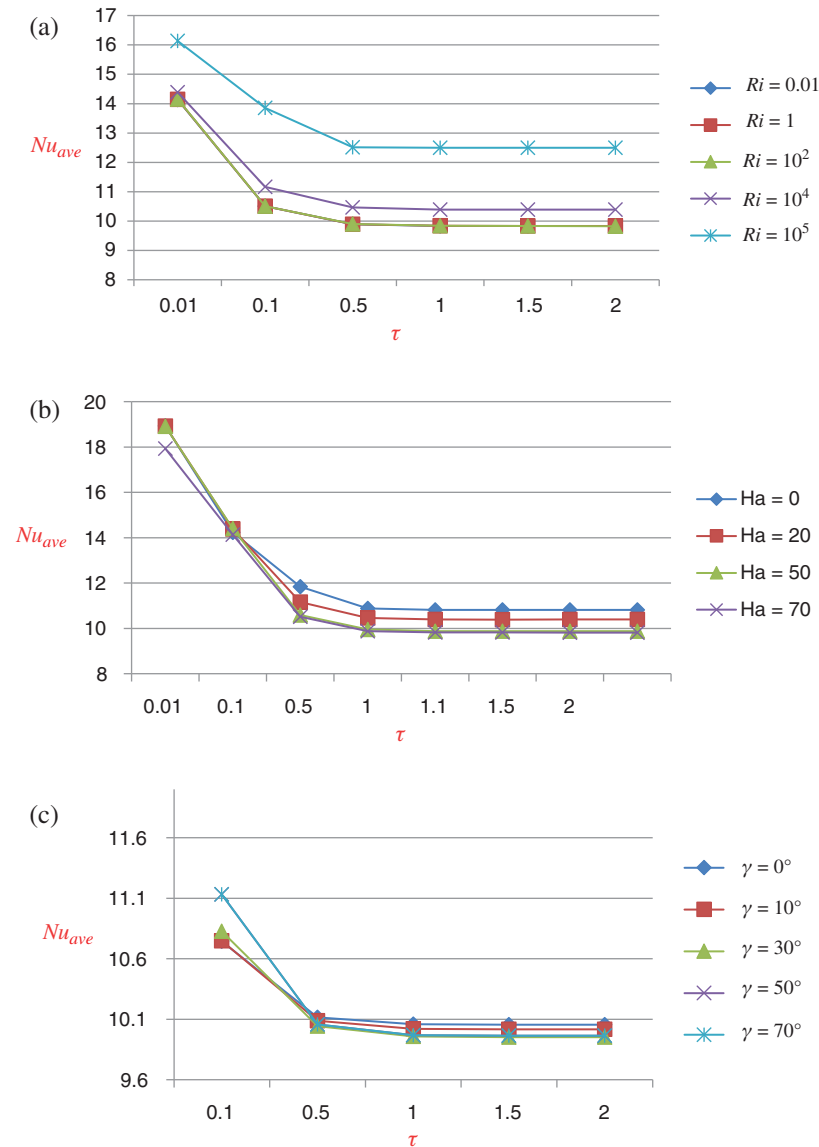


Figure 4: (a)–(c) Average Nusselt number for different value of (a) Ri and τ , (b) Ha and τ , (c) γ and τ when $Pr = 6.838$, $Nb = 1.24 \times 10^{-5}$, $Nt = 9.58 \times 10^{-7}$, $Nr = 0.001$, $Le = 16795$, $AR = 1$

The effects of the orientation of the magnetic field on the average Nusselt number are displayed in Fig. 6. From this figure, we see that Nu_{ave} decreases with the increase of γ when $\gamma < 20$, but a further escalation in γ enhances the rate of heat transfer. Thus, we can say that the magnetic field inclination angle, as well as the Hartmann number, significantly controls the heat transfer rate.

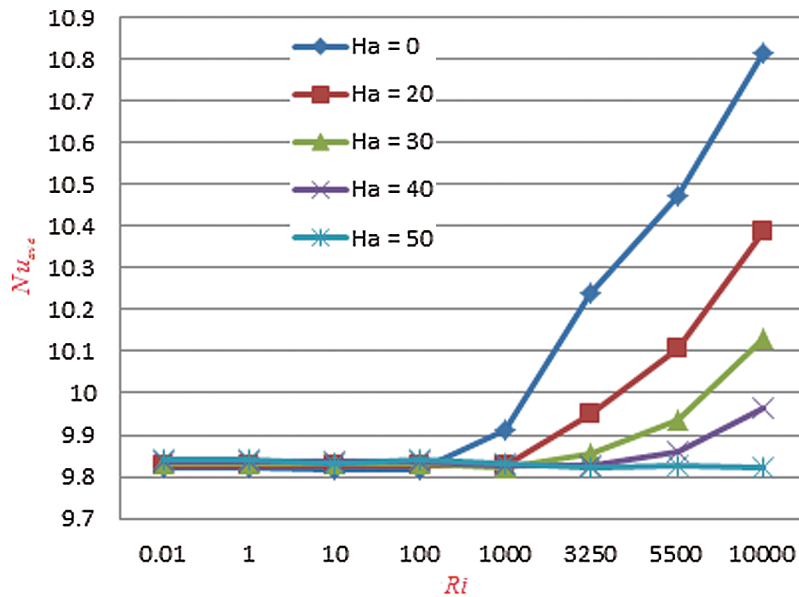


Figure 5: Average Nusselt number for different value of Ha and Ri when $Pr = 6.838$, $Nb = 1.24 \times 10^{-5}$, $Nt = 9.58 \times 10^{-7}$, $Nr = 0.001$, $Le = 16795$, $\gamma = 15^\circ$, $AR = 1$

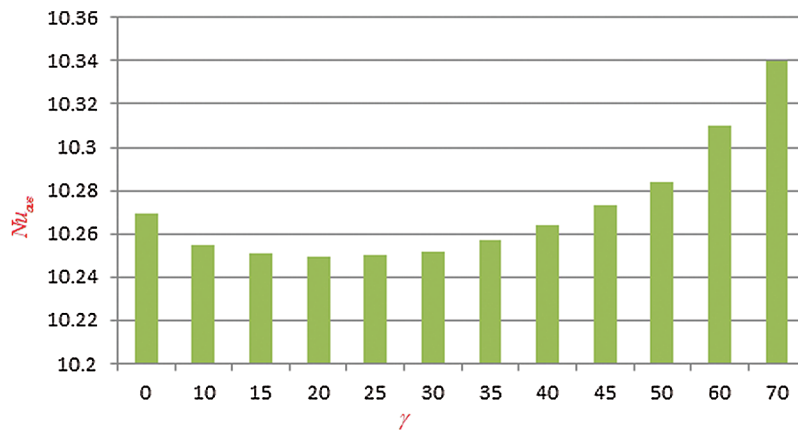


Figure 6: Average Nusselt number for different values of the magnetic field inclination angle γ when $Ri = 10^4$, $Pr = 6.838$, $Nb = 1.24 \times 10^{-5}$, $Nt = 9.58 \times 10^{-7}$, $Nr = 0.001$, $Le = 16795$, $Ha = 25$, and $AR = 1$

One of the most critical characteristics of the problem is the change of the aspect ratio (AR) between the height (the vertical-wall) and length (the horizontal wall) of the triangular enclosure. The diagrams in Fig. 7 show the effect of change in the aspect ratio for different Richardson numbers on the average Nusselt number and resulting heat transfer. As the aspect ratio increases, the average Nusselt number decreases for $AR < 1$. For $AR \geq 1$, the average Nusselt number increases with the increment of AR for all Ri .

We can see from Fig. 8 that changing the aspect ratio has a significant effect on the time required for the solution to reach a steady-state with increasing Richardson number. It is observed from this figure that at the lower value of aspect ratio and for increasing Richardson's number, the solution needs less time to reach a steady-state. Thus, we may conclude that changing the aspect ratio of the triangular enclosure helps the solution reach a steady-state faster with increasing Ri .

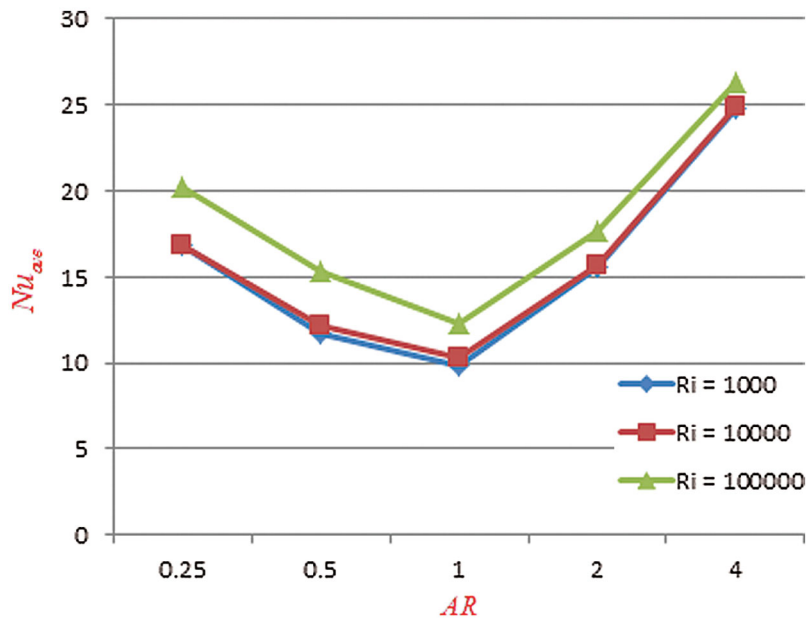


Figure 7: Average Nusselt number for different Richardson number Ri and different aspect ratios AR when $Pr = 6.838$, $Nb = 1.24 \times 10^{-5}$, $Nt = 9.58 \times 10^{-7}$, $Nr = 0.001$, $Le = 16795$, $Ha = 25$, $\gamma = 15^\circ$, $\tau = 2$

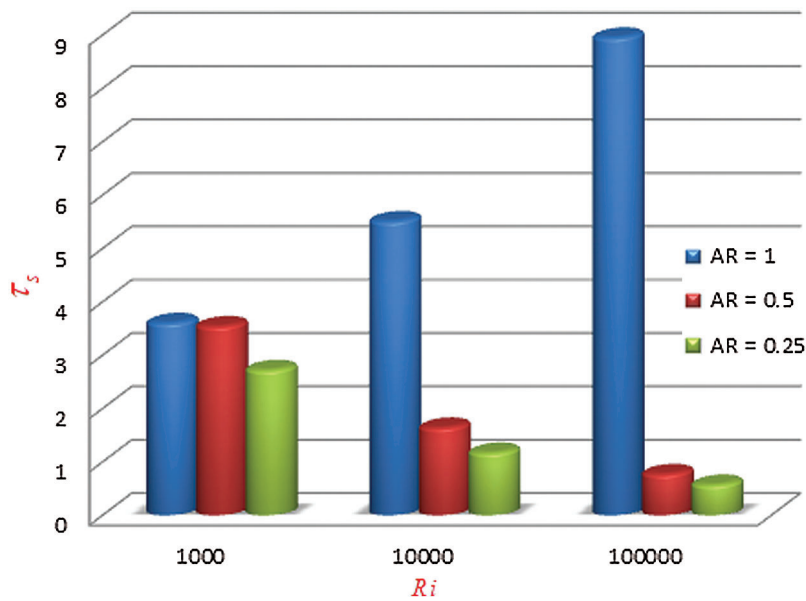


Figure 8: Dimensionless time τ_s needed to reach the solution in steady state for different Richardson number and different aspect ratios when $Pr = 6.838$, $Nb = 1.24 \times 10^{-5}$, $Nt = 9.58 \times 10^{-7}$, $Nr = 0.001$, $Le = 16795$, $Ha = 25$, and $\gamma = 15^\circ$

In our physical model, we have considered that the vertical wall of the triangular enclosure is uniformly heated ($\theta = 1$). But in reality, this configuration may change depending on the specific applications. Thus, it is essential to study the present model taking into the effects of varying the thermal boundary conditions to a non-uniformly heated wall such as $\theta = Y(1 - Y)$ and $\theta = \sin(2\pi Y)$. Consideration of these conditions

further eliminates the discontinuity of the temperature at the top corner of the cavity, where there is a hot and cold wall junction. To study these, we have taken into account the effects of different base fluids such as Kerosene (KE), Ethylene Glycol (EG), and Engine Oil (EO) on the heat transfer mechanisms. Fig. 9 displayed the average Nusselt number for various thermal boundary conditions; Case 1: $\theta = 1$, Case 2: $\theta = Y(1 - Y)$, and Case 3: $\theta = \sin(2\pi Y)$ and for different base fluids (H_2O , Ke, EG, EO) considering Fe_3O_4 nanoparticles when $Ri = 10^4$, $Ha = 25$, $\gamma = 15^\circ$, $AR = 1$, and $\tau = 2$. From this figure, we observe that Case1 gives the highest average Nusselt number comparing to the other two-cases for all types of base fluids. On the other hand, the lowest average Nusselt number we recorded for Case 2. The Fe_3O_4 -EO nanofluid gives the higher rate of heat transfer, whereas, Fe_3O_4 - H_2O has the lowest rate of heat transfer for all three cases of the thermal boundary conditions.

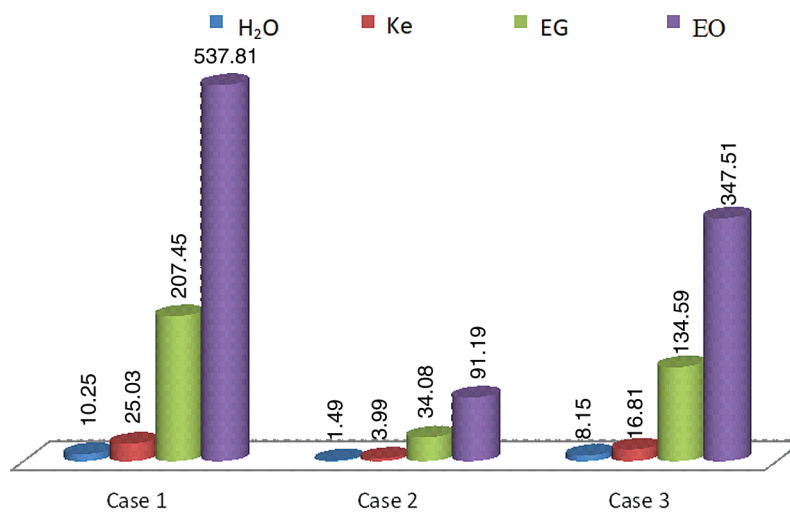


Figure 9: Average Nusselt number for various thermal boundary conditions with different base fluids; H_2O , Ke, EG and EO when $Ri = 10^4$, $Ha = 25$, $\gamma = 15^\circ$, $AR = 1$, and $\tau = 2$. The actual value of the average Nusselt number for EO is divided by 20 to fit within the diagram

Fig. 10 demonstrates the average Nusselt number for various thermal boundary conditions: Case 1, Case 2, and Case 3 with different aspect ratios. As displayed before, Case 1 gives the highest average Nusselt number comparing to the other two-cases for all values of AR. Besides, for all three cases of the thermal boundary conditions, the average Nusselt number decreases with the increase of the aspect ratio. It indicates that the various thermal boundary conditions at the heated wall do not have a significant influence on the aspect ratio of the triangular enclosure.

The average Nusselt number for different aspect ratios with various types of base fluids (H_2O , Ke, EG, and EO) is displayed in Fig. 11. As stated before, the average Nusselt number decreases with the rise of the aspect ratio for all four types of base fluids. Besides, as we observed in Fig. 9, Fe_3O_4 -EO nanofluid gives the highest rate of heat transfer, whereas Fe_3O_4 - H_2O has the lowest heat transfer. So changing the aspect ratio leads to the same trend of heat transfer for different types of base fluids.

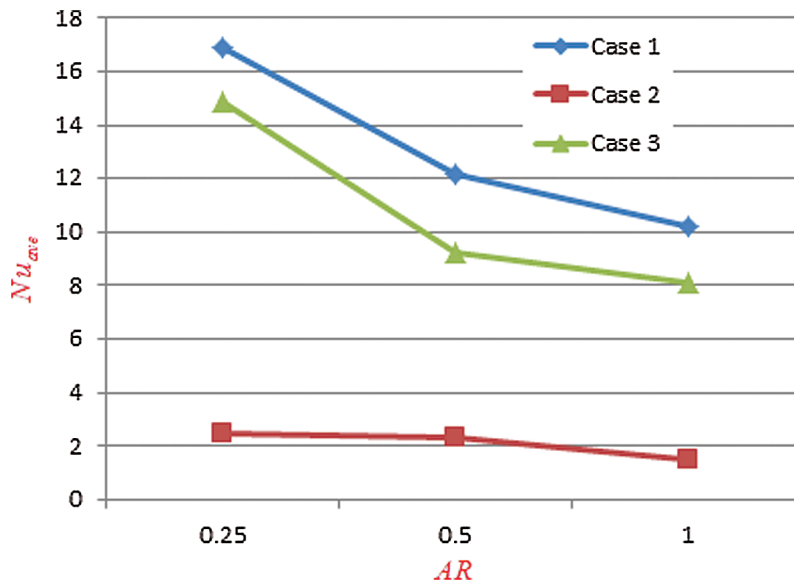


Figure 10: Average Nusselt number for various thermal boundary conditions with different aspect ratio when $Ra = 10^4$, $Pr = 6.838$, $Nb = 1.24 \times 10^{-5}$, $Nt = 9.58 \times 10^{-7}$, $Nr = 0.001$, $Le = 16795$, $Ha = 25$, $\gamma = 15^\circ$, and $\tau = 2$

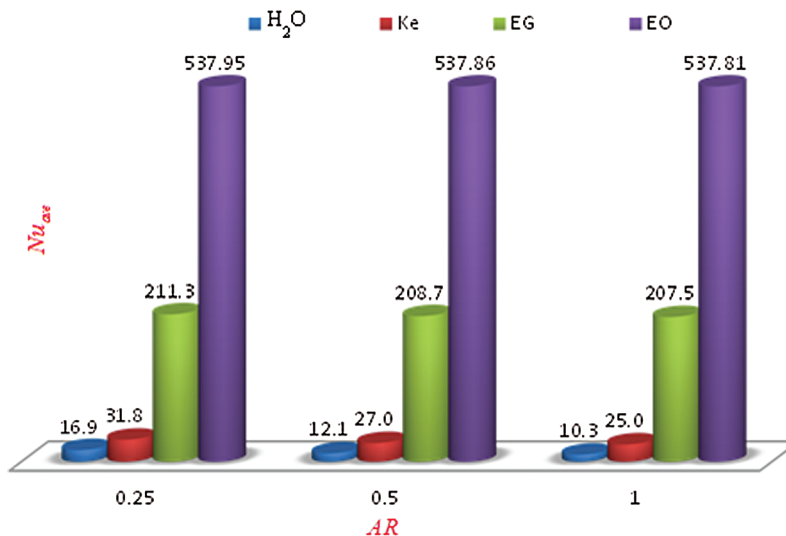


Figure 11: Average Nusselt number for different aspect ratios with various type of base fluids H₂O, Ke, EG and EO when $Ra = 10^4$, $Pr = 6.838$, $Nr = 0.001$, $Ha = 25$, and $\gamma = 15^\circ$, and $\tau = 2$. The actual value of the average Nusselt number for EO is divided by 20 to fit within the diagram

5 Conclusions

In this work, we numerically studied the problem of unsteady natural convection flow and heat transfer in a lid-driven right-angle triangular shaped enclosure filled with Fe₃O₄ nanoparticles in four different types of base fluids such as water, kerosene, ethylene glycol, and engine oil in the presence of an inclined magnetic field. The model used for the binary nanofluid incorporates the effects of Brownian motion and thermophoresis. The influence of changing the thermal boundary conditions of the enclosure was also

investigated, taken into account different aspect ratios of the cavity. Furthermore, we analyzed the time evolution of the solution from unsteady to the steady-state. In the physical model, the effects of the different model parameters such as Richardson number (Ri), Hartmann number (Ha), the inclination angle (γ) of the magnetic field, aspect ratio (AR), and various thermal boundary conditions on the average Nusselt number were investigated in details and discussed their physical significance. From the numerical simulations, we found that a strong magnetic field may suppress the convection mechanisms in nanofluids, as a consequence rate of heat transfer decreases. The magnetic field orientation significantly controls the rate of heat transfer in nanofluids. For the higher value of Ri , the heat transfer rate decreases through lower-values of γ ; but increases through the large-value of γ . The higher Ri confirms better heat transfer through convection than conduction. The heat transfer rate of Fe_3O_4 -EO nanofluid for a uniformly heated wall case is 537.81%, whereas the corresponding rate for the Fe_3O_4 -EG, Fe_3O_4 -Ke and Fe_3O_4 -H₂O nanofluids are 207.45%, 25.03%, and 10.25%, respectively. Again, the heat transfer rate of Fe_3O_4 -EO nanofluid for non-uniformly heated wall case (parabolic case) is 91.19%, whereas the corresponding rates for the Fe_3O_4 -EG, Fe_3O_4 -Ke, and Fe_3O_4 -H₂O nanofluids are 34.08%, 3.99%, and 1.49%, respectively. Finally, the heat transfer rate of Fe_3O_4 -EO nanofluid for a non-uniformly heated wall case (sinusoidal case) is 347.51%, whereas the corresponding rates for the Fe_3O_4 -EG, Fe_3O_4 -Ke, and Fe_3O_4 -H₂O nanofluids are 134.59%, 16.81%, and 8.15%, respectively. Thus, we can conclude that the heat transfer rate strongly depends on the types of nanofluids as well as the types of boundary conditions.

Acknowledgement: M. M. Rahman is grateful to the Sultan Qaboos University for the internal research grant.

Funding Statement: This work was supported by IG/SCI/MATH/20/03.

Conflicts of Interest: The authors declare that there is no conflict of interest.

References

1. Bayomy, A., Saghir, M. Z., Yousefi, T. (2016). Electronic cooling using water flow in aluminum metal foam heat sink: Experimental and numerical approach. *International Journal of Thermal Sciences*, 109, 182–200. DOI 10.1016/j.ijthermalsci.2016.06.007.
2. Choi, S. (1995). Enhancing thermal conductivity of fluids with nanoparticles. In: Signier, D. A., Wang, H. P. (eds.), *Development and applications of non-Newtonian flows. ASME FED*, vol. 231/MD1995; 66, pp. 99–105.
3. Sundar, L. S., Naik, M. T., Sharma, K. V., Singh, M. K., Reddy, T. C. S. (2012). Experimental investigation of forced convection heat transfer and friction factor in a tube with Fe_3O_4 magnetic nanofluid. *Experimental Thermal and Fluid Science*, 37, 65–71. DOI 10.1016/j.expthermflusci.2011.10.004.
4. Bayomy, A. M., Saghir, M. Z. (2017). Experimental study of using γ - Al_2O_3 -water nanofluid flow through aluminum foam heat sink: Comparison with numerical approach. *International Journal of Heat and Mass Transfer*, 107, 181–203. DOI 10.1016/j.ijheatmasstransfer.2016.11.037.
5. Saghir, M. Z., Welsford, C., Thanapathy, P., Bayomy, A. M., Delisle, C. (2020). Experimental measurements and numerical computation of nano heat transfer enhancement inside a porous material. *Journal of Thermal Science and Engineering Applications*, 12(1), 1023. DOI 10.1115/1.4041936.
6. Alhajaj, Z., Bayomy, A. M., Saghir, M. Z., Rahman, M. M. (2020). Flow of nanofluid and hybrid fluid in porous channels: Experimental and numerical approach. *International Journal of Thermofluids*, 1–2, 100016. DOI 10.1016/j.ijft.2020.100016.
7. Ho, C. J., Chen, W. C. (2013). An experimental study on thermal performance of Al_2O_3 /water nanofluid in a minichannel heat sink. *Applied Thermal Engineering*, 50(1), 516–522. DOI 10.1016/j.applthermaleng.2012.07.037.
8. Nabil, M. F., Azmi, W. H., Hamid, K. A., Mamat, R., Hagos, F. Y. (2017). An experimental study on the thermal conductivity and dynamic viscosity of TiO_2 - SiO_2 nanofluids in water: Ethylene glycol mixture. *International Communications in Heat and Mass Transfer*, 86, 181–189. DOI 10.1016/j.icheatmasstransfer.2017.05.024.
9. Buongiorno, J. (2006). Convective transport in nanofluids. *Journal of Heat Transfer*, 128(3), 240–250. DOI 10.1115/1.2150834.

10. Wang, X., Xu, X., Choi, S. U. (1999). Thermal conductivity of nanoparticle-fluid mixture. *Journal of Thermophysics and Heat Transfer*, 13(4), 474–480. DOI 10.2514/2.6486.
11. Xuan, Y., Li, Q. (2003). Investigation on convective heat transfer and flow features of nanofluids. *Journal of Heat Transfer*, 125(1), 151–155. DOI 10.1115/1.1532008.
12. Eastman, J. A., Phillpot, S. R., Choi, S. U. S., Keblinski, P. (2004). Thermal transport in nanofluids. *Annual Review Materials Research*, 34(1), 219–246. DOI 10.1146/annurev.matsci.34.052803.090621.
13. Jalali, H., Abbassi, H. (2020). Analysis of the influence of viscosity and thermal conductivity on heat transfer by Al₂O₃-water nanofluid. *Fluid Dynamics & Materials Processing*, 16(2), 181–198. DOI 10.32604/fdmp.2020.07804.
14. Khanafer, K., Vafai, K., Lightstone, M. (2003). Buoyancy-driven heat transfer enhancement in a two-dimensional enclosure utilizing nanofluids. *International Journal of Heat and Mass Transfer*, 46(19), 3639–3653. DOI 10.1016/S0017-9310(03)00156-X.
15. Oztop, H. F., Abu-Nada, E. (2008). Numerical study of natural convection in partially heated rectangular enclosures filled with nanofluids. *International Journal of Heat and Fluid Flow*, 29(5), 1326–1336. DOI 10.1016/j.ijheatfluidflow.2008.04.009.
16. Chamkha, A. J. (2002). Hydromagnetic combined convection flow in a vertical lid-driven cavity with internal heat generation or absorption. *Numerical Heat Transfer, Part A: Applications*, 41(5), 529–546. DOI 10.1080/104077802753570356.
17. Rahman, M. M., Alim, M. A., Sarker, M. M. A. (2010). Numerical study on the conjugate effect of joule heating and magneto-hydrodynamics mixed convection in an obstructed lid-driven square cavity. *International Communications in Heat and Mass Transfer*, 37(5), 524–534. DOI 10.1016/j.icheatmasstransfer.2009.12.012.
18. Malleswaran, A., Sivasankaran, S. (2016). A numerical simulation on MHD mixed convection in a Lid-driven cavity with corner heaters. *Journal of Applied Fluid Mechanics*, 9(1), 311–319. DOI 10.18869/acadpub.jafm.68.224.22903.
19. Al Kalbani, K. S., Alam, M. S., Rahman, M. M. (2016). Finite element analysis of unsteady natural convective heat transfer and fluid flow of nanofluids inside a tilted square enclosure in the presence of oriented magnetic field. *American Journal of Heat and Mass Transfer*, 3(3), 186–224.
20. Al Kalbani, K. S., Rahman, M. M., Alam, S., Al-Salti, N., Eltayeb, I. A. (2017). Buoyancy induced heat transfer flow inside a tilted square enclosure filled with nanofluids in the presence of oriented magnetic field. *Heat Transfer Engineering*, 39(6), 511–525. DOI 10.1080/01457632.2017.1320164.
21. Al Balushi, L. M., Rahman, M. M. (2019). Convective heat transfer utilizing magnetic nanoparticles in the presence of a sloping magnetic field inside a square enclosure. *Journal of Thermal Science and Engineering Applications*, 11(4), 99. DOI 10.1115/1.4044120.
22. Al Balushi, L. M., Rahman, M. M. (2020). Impacts of heat flux distribution, sloping magnetic field and magnetic nanoparticles on the natural convective flow contained in a square cavity. *Fluid Dynamics & Material Processing*, 16(3), 441–463. DOI 10.32604/fdmp.2020.08551.
23. Koseff, J. R., Prasad, A. K. (1984). The lid-driven cavity flow: A synthesis of quantitative and qualitative observations. *Journal of Fluids Engineering*, 106(4), 390–398. DOI 10.1115/1.3243136.
24. Flack, R. D., Konopnicki, T., Rooke, J. H. (1979). The measurement of natural convective heat transfer in triangular enclosures. *Journal of Heat Transfer*, 101, 770–772.
25. Flack, R. D. (1980). The experimental measurement of natural convection heat transfer in triangular enclosures heated or cooled from below. *Journal of Heat Transfer*, 102(4), 770–772. DOI 10.1115/1.3244389.
26. Akinsete, V. A., Coleman, T. A. (1982). Heat transfer by steady laminar free convection in triangular enclosures. *International Journal of Heat and Mass Transfer*, 25(7), 991–998. DOI 10.1016/0017-9310(82)90074-6.
27. Ridouane, E. I., Campo, A., Chang, J. Y. (2005). Natural convection patterns in right-angled triangular cavities with heated vertical sides and cooled hypotenuses. *Journal of Heat Transfer*, 127(10), 1181–1186. DOI 10.1115/1.2033903.
28. Varol, Y., Oztop, H. F., Varol, A. (2007). Effects of thin fin on natural convection in porous triangular enclosures. *International Journal of Thermal Sciences*, 46(10), 1033–1045. DOI 10.1016/j.ijthermalsci.2006.11.001.

29. Basak, T., Aravind, G., Roy, S. (2009). Visualization of heat flow due to natural convection within triangular cavities using Bejan's heatline concept. *International Journal of Heat and Mass Transfer*, 52(11–12), 2824–2833. DOI 10.1016/j.ijheatmasstransfer.2008.10.034.
30. Yesiloz, G., Aydin, O. (2013). Laminar natural convection in right-angled triangular enclosures heated and cooled on adjacent walls. *International Journal of Heat and Mass Transfer*, 60, 365–374. DOI 10.1016/j.ijheatmasstransfer.2013.01.009.
31. Triveni, M. K., Panua, R. (2018). Numerical study of natural convection in a right triangular enclosure with sinusoidal hot wall and different configurations of cold wall. *Fluid Dynamics and Materials Processing*, 14(1), 1–21.
32. Ghasemi, B., Aminossadati, S. M. (2010). Brownian motion of nanoparticles in a triangular enclosure with natural convection. *International Journal of Thermal Sciences*, 49(6), 931–940. DOI 10.1016/j.ijthermalsci.2009.12.017.
33. Ghasemi, B., Aminossadati, S. M. (2010). Mixed convection in a lid-driven triangular enclosure filled with nanofluids. *International Communications in Heat and Mass Transfer*, 37(8), 1142–1148. DOI 10.1016/j.icheatmasstransfer.2010.06.020.
34. Rahman, M. M., Alam, M. S., Al-Salti, N., Eltayeb, I. A. (2016). Hydromagnetic natural convective heat transfer flow in an isosceles triangular cavity filled with nanofluid using two-component nonhomogeneous model. *International Journal of Thermal Sciences*, 107, 272–288. DOI 10.1016/j.ijthermalsci.2016.04.009.
35. Rahman, M. M. (2016). Influence of oriented magnetic field on natural convection in an equilateral triangular enclosure filled with water-and kerosene-based ferrofluids using a two-component nonhomogeneous thermal equilibrium model. *Cogent Physics*, 3(1), 1234662.
36. Rahman, M. M. (2018). Heat transfer in $\text{Fe}_3\text{O}_4\text{-H}_2\text{O}$ nanofluid contained in a triangular cavity under a sloping magnetic field. *Sultan Qaboos University Journal for Science*, 23(1), 56–67. DOI 10.24200/squjs.vol23iss1pp56-67.
37. Azam, M., Khan, M., Alshomrani, A. S. (2017). Unsteady radiative stagnation point flow of MHD Carreau nanofluid over expanding/contracting cylinder. *International Journal of Mechanical Sciences*, 130, 64–73. DOI 10.1016/j.ijmecsci.2017.06.010.
38. Azam, M., Khan, M. (2017). Unsteady heat and mass transfer mechanisms in MHD Carreau nanofluid flow. *Journal of Molecular Liquids*, 225, 554–562. DOI 10.1016/j.molliq.2016.11.107.
39. Azam, M., Shakoor, A., Rasool, H. F., Khan, M. (2019). Numerical simulation for solar energy aspects on unsteady convective flow of MHD Cross nanofluid: A revised approach. *International Journal of Heat and Mass Transfer*, 131, 495–505. DOI 10.1016/j.ijheatmasstransfer.2018.11.022.
40. Azam, M., Xu, T., Shakoor, A., Khan, M. (2020). Effects of Arrhenius activation energy in development of covalent bonding in axisymmetric flow of radiative-Cross nanofluid. *International Communications in Heat and Mass Transfer*, 113, 104547. DOI 10.1016/j.icheatmasstransfer.2020.104547.
41. Azam, M., Xu, T., Khan, M. (2020). Numerical simulation for variable thermal properties and heat source/sink in flow of Cross nanofluid over a moving cylinder. *International Communications in Heat and Mass Transfer*, 118, 104832. DOI 10.1016/j.icheatmasstransfer.2020.104832.
42. Uddin, M. J., Rahman, M. M. (2020). Heat transportation in Copper Oxide-water nanofluid filled triangular cavities. *International Journal of Heat and Technology*, 38(1), 106–124. DOI 10.18280/ijht.380112.
43. Reddy, J. N., Gartling, D. K. (2010). *The finite element method in heat transfer and fluid dynamics*, 3rd Edition. Boca Raton, Florida: CRC Press.
44. Uddin, M. J., Rahman, M. M. (2018). Finite element computational procedure for convective flow of nanofluids in an annulus. *Thermal Science and Engineering Progress*, 6, 251–267. DOI 10.1016/j.tsep.2018.04.011.
45. Uddin, M., Kalbani, K. S. A., Rahman, M. M., Alam, M. S., Al-Salti, N. et al. (2016). Fundamentals of nanofluids: Evolution, applications and new theory. *Journal of Biomathematics and Systems Biology*, 2(1), 1–32.
46. Myers, T. G., Ribera, H., Cregan, V. (2017). Does mathematics contribute to the nanofluid debate? *International Journal of Heat and Mass Transfer*, 111, 279–288. DOI 10.1016/j.ijheatmasstransfer.2017.03.118.